MGL/SiNW-based exotic *pin* switch with low insertion loss and high isolation for THz communication: a quantum-rectified Schrodinger–Poisson drift-diffusion model for the design and analysis of switching behavior

Saunak Bhattacharya[1], Abhijit Kundu[1]*, Jhuma Kundu[2], Angsuman Sarkar[3] and Moumita Mukherjee[4]

[1]Department of Electronics & Communication Engineering, Chaibasa Engineering College, Jharkhand, India, [2]Department of Electronics & Communication Engineering, NSHM Knowledge Campus, Durgapur, West Bengal, India, [3]Department of Electronics & Communication Engineering, Kalyani Govt. Engineering College, Kalyani, India, [4]Department of Physics, Adamas University, Kolkata, India

In this paper, the authors explore the potential of an exotic multi-graphene layer/ Si nanowire (MGL/SiNW) *pin* device as a switch in the THz frequency domain. The device is developed by the incorporation of multiple SiNWs into its intrinsic region. In contrast, cap and bottom layers are developed by the incorporation of multiple graphene layers. The electrical characterization of the proposed exotic *pin* device is carried out by developing a quantum-rectified Schrodinger–Poisson drift-diffusion (QRSP-DD) model. The developed QRSP-DD model is validated by analyzing experimental and simulation observations under similar operating conditions. After establishing its validity, the same model in conjunction with the PSpice simulator is used to obtain the switching characteristics of MGL/SiNW *pin*-based series-shunt and shunt single-pole single-throw (SPST), single-pole double-throw (SPDT), and single-pole multiple-throw (SPMT) switches in the THz frequency domain. The analysis proves that the MGL/SiNW *pin*-based SPMT switch offers low resistance (0.56 Ω), high isolation (91.15 dB), and low insertion loss (0.007 dB) at 5 THz frequency compared to its SiNW counterpart.

KEYWORDS

multi-graphene layer/Si nanowire, quantum rectified Schrodinger–Poisson drift-diffusion model, RF series resistance, insertion loss, isolation

1 Introduction

In recent years, device engineers have shown a remarkable increase in research interest in developing high-frequency switches due to their extensive applications in modern communication and defense sectors (Mamedes and Bornemann, 2021; Pratt and Oliver, 2021; Xu et al., 2021; Kundu et al., 2021a; Kundu et al., 2018; Paz-Martínez et al., 2021). The effective utilization of the sub-THz/MMW spectrum results in the development of high-performance active and passive devices, which are often expensive to fabricate. *pin* switches are the most powerful devices among RF switches, capable of controlling high-frequency RF signals with low DC current and voltage. Several studies investigated the switching characteristics of various materials and structures in *pin* switches, focusing on insertion loss and isolation within the frequency range of 1–100 GHz. The values of these two parameters do not significantly enhance device performance in the high-frequency region. It is observed from the reported research work that the size miniaturization and development of cost-effective, highly sensitive THz switches with low insertion loss and high isolation are still in the experimental stage (Buder et al., 2003; Camara and Zekentes, 2006; Kundu et al., 2019; Pinping et al., 2005; Pratt and Oliver, 2021; Yang et al., 2005; Kundu and Mukherjee, 2022). It is clear from the literature review that no report is available on multi-graphene layer/Si nanowire (MGL/SiNW)-based exotic pin switches at terahertz frequency.

Hence, there is a wide scope for improvement in the device performance by changing its geometric structure. Among different types of solid-state and electromechanical switches, pin-based switches are generally in demand for THz communication to date (Kundu et al., 2018; Paz-Martínez et al., 2021). The pin device consists of a lightly doped i-region between the heavily doped p and n regions. The lightly doped i-region plays an important role in handling large RF signals (Hadi et al., 2013). Hence, the doping concentration and the geometric structure of the i-region are the two essential factors for developing a pin-based THz-switch with low insertion loss and high isolation.

In this research work, the authors have investigated the switching properties of MGL/SiNW pin-based series-shunt and shunt single-pole single-throw (SPST), single-pole double-throw (SPDT), and single-pole multiple-throw (SPMT) switches in the THz frequency range. The miniaturized size of the device with low power consumption can be achieved by the incorporation of nanowires in the active region of the device. In nanowire devices, the energy band structure can be reformed due to its high surface area per unit volume (Ng et al., 2007). This phenomenon increases the electrical properties of the device to a certain level. As a result, the overall performance of the device is significantly enhanced (Tomioka et al., 2009; Tomioka et al., 2011). Due to the applied RF signal, the induced electric field excites the electron to move from the lower energy band to the higher energy band. The flow of the charged particles in the device depends on the amount of the applied RF signal. The overall performance of the device can be significantly enhanced by reducing internal RF resistance through band-bending engineering.

From the literature review, it has been observed that the switching properties of the conventional device can be obtained by solving the classical drift-diffusion model (Takahashi et al.,
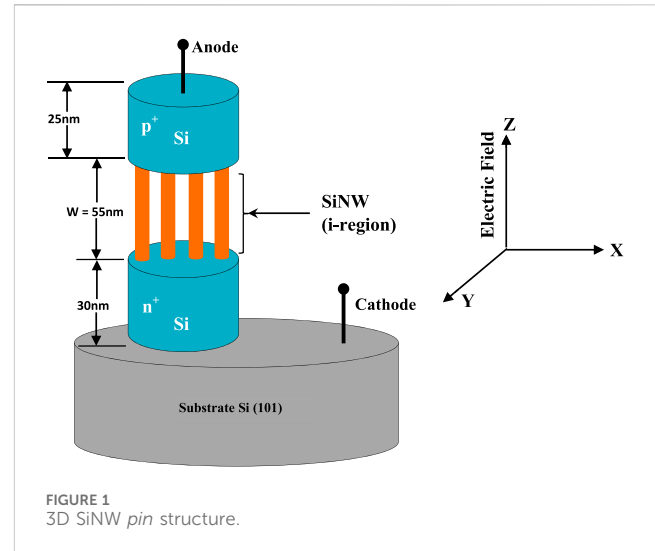
FIGURE 1
3D SiNW *pin* structure.
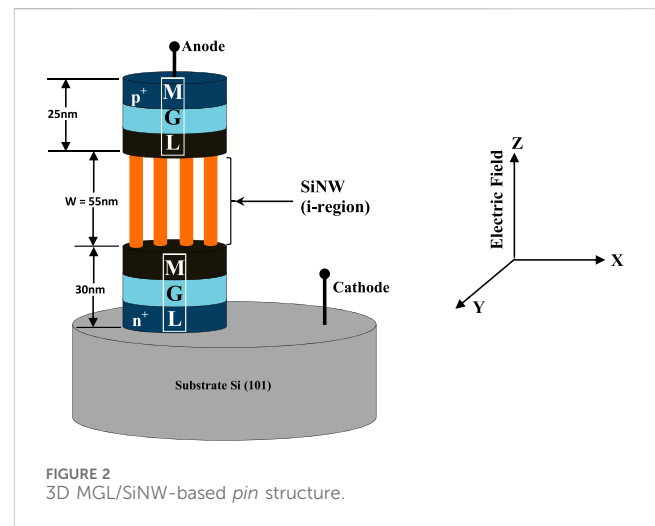
FIGURE 2
3D MGL/SiNW-based *pin* structure.

2011; Bellantoni et al., 1989; Boles et al., 2013; Egorov et al., 2018). Due to their miniature size, nanowire structures exhibit exceptional phenomena that cannot be described by the classical model. Therefore, in the case of nanowire devices, the switching characteristics are analyzed by the incorporation of necessary quantum correction to the classical drift-diffusion model. The quantum-rectified drift-diffusion (DD) model is developed by the inclusion of Bohm potential into the Schrodinger–Poisson equation. This quantum-rectified Schrodinger–Poisson DD model (QRSP-DD) is used to analyze the switching properties in device modeling with the appropriate boundary conditions. The validation of the developed QRSP-DD model is implemented through a comparability study of simulated and experimental results, retaining the variables (operating frequency, temperature, and electrical parameters) constant (Bogle et al., 2010; Henfiner et al., 2001). The performance of the device under test (DUT) is compared with that of the conventional Si nanowire counterpart. The geometric structure of the Si nanowire (SiNW) pin device is shown in Figure 1. In contrast, the geometric structure of the MGL/SiNW pin device is shown in Figure 2. It is observed from the geometric structure of

TABLE 1 Required design parameters of the proposed nanowire *pin* devices.

Type of nanowire device	Operating frequency in the THz domain	Intrinsic region parameter			Parameter of the top and bottom layers			
		Width (W) (nm)	Diameter (nm)	Doping concentration (N$_d$) (m^{-3})	Doping concentration of the bottom layer (n region) (N$_n^{++}$) (10^{23}) (m^{-3})	Doping concentration of the top layer (p region) (N$_p^{++}$) (10^{22}) (m^{-3})	Width of the bottom layer (n region)	Width of the top layer (p region)
SiNW *pin* switch	1–12	55	11	1×10^{17}	2.5	3.5	30	25
MGL/SiNW *pin* switch	1–12	55	11	5×10^{18}	3.5	4.5	30	25

MGL/SiNW devices that the p and n regions are made up of multiple graphene layers. Due to the inclusion of the multiple graphene layers into the p and n regions, the effective mobility of the charged particles in the p and n regions increases significantly (Novoselov et al., 2004; Oberlin et al., 1976; Johon et al., 2004). The design parameters of the device are calculated from the transit time phenomenon through several iterations in a computer program (Table 1). After developing the MGL/SiNW exotic pin device, the authors have designed and analyzed the switching performance of series shunt and shunt SPST, SPDT, and SPMT switches in the THz frequency domain in terms of insertion loss and isolation. The switching configurations of series shunt and shunt SPST, SPDT, and SPMT switches are shown in Figures 3A–D. The novelty of this research lies in the size miniaturization and the use of multiple graphene layers for the cap and bottom layers of the structure, which result in low power consumption, low insertion loss, and high isolation at THz frequencies.

2 Device modeling

This section describes the device modeling for the design and analysis of the switching characteristics of MGL/SiNW exotic pin switches in the THz frequency region. The non-linear RF characteristics of the device at THz frequencies are analyzed through the development of the QRSP-DD model by considering appropriate boundary conditions, simulation techniques, and the device's structure details. The development of the QRSP-DD model, its design parameters, and non-linear RF characteristics are discussed in detail in Sections 2.1, 2.2, and 2.3 respectively.

2.1 Quantum-rectified Schrodinger−Poisson drift-diffusion model

The QRSP-DD model is developed based on the solutions to the Schrodinger–Poisson equation, in which quantum-potential (QP) is incorporated, and it can be expressed as (Falco et al., 2005)

$$\left(\frac{\hbar^2}{2m_{ef}^*(z)} \nabla^2 + V_{ef}(z) \right) \psi(x, y, z) + E_{ef}(z)\psi(x, y, z) = E\psi(x, y, z).$$

(1)
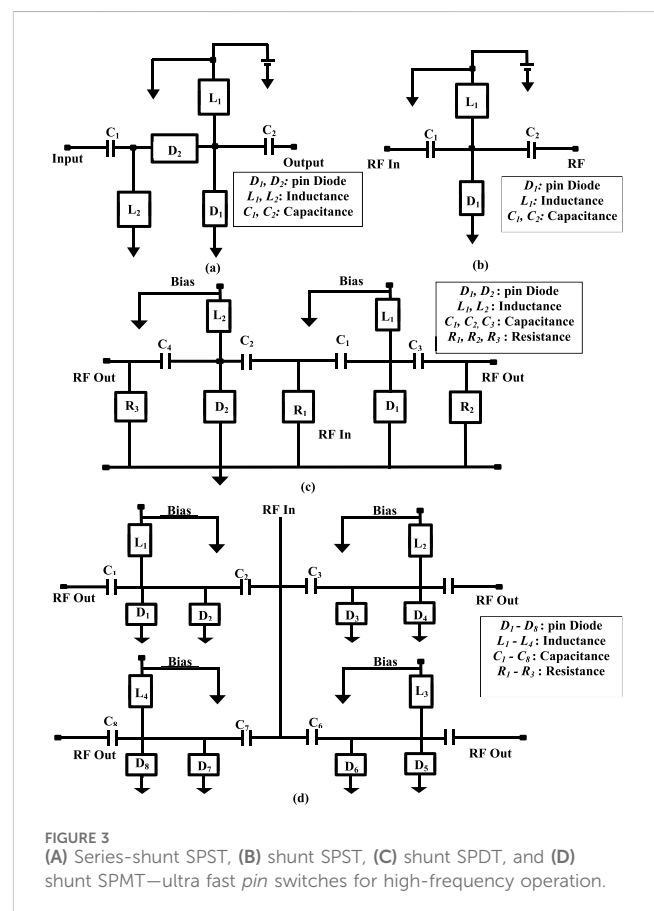
FIGURE 3
(A) Series-shunt SPST, (B) shunt SPST, (C) shunt SPDT, and (D) shunt SPMT—ultra fast *pin* switches for high-frequency operation.

In the intrinsic region, the effective mass of electron and hole changes along the z-axis, as depicted in Figures 1A, B. The working principle of the pin switch can be properly explained under biasing conditions. The switch reaches its 'ON' and 'OFF' state under forward bias and reverse bias conditions, respectively. Consequently, the effect of the biasing voltage ($V_{ef}(z)$) is incorporated into Equation 1. However, the Schrodinger equation is modified by the inclusion of an effective energy term into Equation 1, as provided by Falco et al. (2005).

$$E_{ef}(z) = -e\left[\phi(z) + B_n^{QCDD} \right] + \frac{E_g}{2} + kTln\sqrt{\frac{N_c}{N_v}} + E_{def}(z).$$

(2)

In Equation 2, n_c and n_v represent the effective density state of the conduction band and valence band, respectively, and $\phi(z)$ represents the effective potential. B_n^{QCDD} represents the Bohm potential, which is given by Equation 3.

$$B_n^{QCDD} = \delta_n^2 \frac{\nabla(\nabla\sqrt{n})}{\sqrt{n}}, \qquad (3)$$

where n is the concentration of the negatively charged carrier and can be represented as Equation 4.

$$n = \exp\left(\left(\varphi + B_n^{QCDD}\right) - \varphi_n\right). \qquad (4)$$

In device modeling, the moderately doped intrinsic region and heavily doped p and n regions are divided into barriers and wells. Subsequently, the Schrodinger–Poisson equation can be expressed in the following form.

$$\left(-\frac{\hbar^2}{2m_{efz}^{*W_{wl}/B_r}}\frac{\partial^2}{\partial z^2} + V_n^{W_{wl}/B_r} + \frac{\hbar^2\left(k_{inplane}\right)^2}{2m_{ef(x,y)}^{*W_{wl}/B_r}}\right)\gamma_n^{W_{wl}/B_r}(z)$$
$$+ E_{ef}^{W_{wl}/B_r}\gamma_n^{W_{wl}/B_r}(z)$$
$$= E\gamma_n^{W_{wl}/B_r}(z). \qquad (5)$$

In Equation 5, W_{wl} and B_r represent well and barrier in the device, respectively.

The kinetic energy term is split into two components: *i.* out-of-plane component and *ii.* in-plane component. The out-of-plane component is represented by $\left(-\frac{\hbar^2}{2m_{ef}^{*W_{wl}/B_r}}\frac{\partial^2}{\partial z^2}\right)$, and the in-plane component is represented by $\left(2m_{ef(x,y)}^{*W_{wl}/B_r}\right)$. Due to the inclusion of multiple nanowires into the intrinsic region, the conduction band splits into two segments. In the in-plane components, $k_{inplane} = k_x, k_y$.

The actual energy for well and barrier can be written as shown in Equation 6.

$$E_{ef}(z) = \begin{cases} E_{ef}^W = \left(-e\left[\varphi(z) + B_n^{QCDD}\right] + \frac{E_G}{2} + kT\ln\sqrt{\frac{N_c}{N_v}}\right)\bigg|_{W_{wl}} \\ \quad + E_{def}^{W_{wl}} \text{ at well} - \text{region} \\ E_{ef}^B = \left(-e\left[\varphi(z) + B_n^{QCDD}\right] + \frac{E_G}{2} + kT\ln\sqrt{\frac{N_c}{N_v}}\right)\bigg|_{B_r} \\ \quad + E_{def}^{B_r} \text{ at barrier} - \text{region} \end{cases} . \quad (6)$$

During device modeling, the change in the effective potential in well and barrier regions of the device can be obtained by Equation 7.

$$V_{ef}(z) = \begin{cases} V_n^{W_{wl}} = 0 \text{ at well} - \text{region} \\ V_n^{B_r} = \Delta E_C^{offset} \text{ at barrier} - \text{region} \end{cases}, \qquad (7)$$

where ΔE_C^{offset} is the offset present in the conduction band.

The effective mass of the charged carriers in the well and barrier regions along in-plane and out-of-plane directions is given by (Greve, 2001; Ang et al., 2004) Equations 8a, 8b respectively.

$$m_{ef(x,y)}^*(z) = \begin{cases} m_{ef(x,y)}^{*W_{wl}} \text{ in well region} \\ m_{ef(x,y)}^{*B_r} \text{ in barrier region} \end{cases}, \qquad (8a)$$

$$m_{efz}^*(z) = \begin{cases} m_{efz}^{*W_{wl}} \text{ in well region} \\ m_{efz}^{*B_r} \text{ in barrier region} \end{cases}. \qquad (8b)$$

In this device modeling, the wave function is represented by

$$\psi(x,y,z) = f_n(x,y,z)q_n(x,y,z)|_{k=0}. \qquad (9)$$

In Equation 9, the periodicity of the Bloch function is denoted by $q_n(x,y,z)|_{k=0}$. In the case of nanowire structures, the term $f_n(x,y,z)$ can be substituted with $f_n^{W_{wl}/B_r}(r,z)$ by considering the well and barrier components, and it is given by Equation 10.

$$f_n^{W_{wl}/B_r}(r,z) = \frac{1}{\sqrt{S}}e^{ik_{inplane}\cdot r}\gamma_n^{W_{wl}/B_r}(z), \qquad (10)$$

where $r \in x, y$ and $k_{inplane} = k_x, k_y$.

In Equation 5, the inclusion of position reliant effective mass $(m_{efz}^*(z))$ allows the substitution of non-Hermitian kinetic energy operator with its Hermitian counterpart. This substitution is further modified into Ben Daniel–Duke equation.

$$\left(-\frac{\hbar^2}{2}\frac{\partial}{\partial z}\frac{1}{m_{efz}^*}\frac{\partial}{\partial z} + \frac{\hbar^2\left(k_{inplane}\right)^2}{2m_{ef(x,y)}^{*W_{wl}/B_r}} + V_n^{W_{wl}/B_r}\right)\gamma_n^{W_{wl}/B_r}(z)$$
$$+ E_{eff}^{W_{wl}/B_r}\gamma_n^{W_{wl}/B_r}(z)$$
$$= E\gamma_n^{W_{wl}/B_r}(z). \qquad (11)$$

Applying the Ben Daniel–Duke boundary conditions, Equation 11 can be modified as

$$\gamma_n(z), \frac{1}{m_{ef}^*}\frac{\partial\gamma_n(z)}{\partial z}\epsilon \text{ continuous.} \qquad (12)$$

The assumption made in Equation 12 can be proven true as the total wave function, $\psi(x,y,z)$, is continuous at the interfaces. Furthermore, the periodic part of the Bloch function in well and barrier regions is assumed to be identical, and it can be represented as

$$q_n(x,y,z)|_{k=0}^A = q_n(x,y,z)|_{k=0}^B. \qquad (13)$$

The presumption made in Equation 13 affects the continuity of $\frac{1}{m_{ef}^*}\frac{\partial\gamma_n(z)}{\partial z}$ under the conservation of current. In the heterocrystalline MGL/SiNW pin device, the effective density of states is represented by the solutions to Equation 11, which can be described as follows:

$$\left(-\frac{\hbar^2}{2m_{efz}^*}\frac{\partial^2}{\partial z^2} + V_n + \frac{\hbar^2\left(k_{inplane}\right)^2}{2m_{ef(x,y)}^*}\right)\gamma_n(z) + E_{ef}\gamma_n(z) = E\gamma_n(z).$$
$$(14)$$

In Equation 14, m_n^* represents the effective mass of the electron. Furthermore, the 3-D density state of energy for the heterocrystalline MGL/SiNW device is obtained from Equation 15, which can be expressed as

$$g(E) = \frac{2}{volume}\sum_{l_m,\varphi,k_{inplane}}\delta\left(E - E\left(l_m,\varphi,k_{inplane}\right)\right)$$
$$= \frac{m_{efz}^*}{\pi^2\hbar^2}\sum_{l_m}\int_0^{\pi/t_s}U_{unit-s}\left(E - E_{l_m}(\varphi)\right)d\varphi. \qquad (15)$$

Now, Equation 15 is solved by incorporating the appropriate boundary conditions, i.e., $E < E_{minimum}$, $E_{min} < E < E_{maximum}$, and $E_{maximum} < E$. Finally, the energy density function can be expressed as

$$g(E) = \begin{cases} 0 & E < E_{minimum} \\ \dfrac{m^*_{efz}}{\pi^2 h^2} \dfrac{\varphi(E)}{d} & E_{minimum} < E < E_{maximum} \\ \dfrac{m^*_{efz}}{\pi^2 h^2} E_{maximum} \langle E \end{cases}, \quad (16)$$

where d is the number of nanowires, $\varphi(E)$ is the wave vector, l_m is the position of the miniband, and $U_{unit\text{-}s}$ is the unit step function. The range of the energy in l_m is between $E_{minimum}$ and $E_{maximum}$. The charged carrier's concentration is an important attribute of the device, and it can be determined by

$$C_{h,e}(z,t) = \int_{E_C}^{\infty} g(E) f(E) dE. \quad (17)$$

In Equation 17, $f(E)$ denotes the occupation probability of the density function. The concentration of the charged carrier ($C_{p,n}(z,t)$) is incorporated into the carrier transport equations (i.e., Poisson's equation, current density equation, and continuity equation) and can be expressed as (Sze, 2008; Kundu et al., 2021b) Equation 18.

$$\frac{\partial^2}{\partial z^2} V(z,t) = -\frac{e}{\varepsilon}(n_d - n_a + C_h(z,t) - C_e(z,t)), \quad (18)$$

$$J_{h,e} = -e\mu_{h,e}\left(C_{h,e}(z,t)\frac{\partial}{\partial z}V(z,t) \pm \frac{kT}{q}\frac{\partial}{\partial z}C_{h,e}(z,t) + B_n^{QCDD}(z,t)\right), \quad (19)$$

$$\frac{\partial}{\partial z}C_{h,e}(z,t) = -\frac{1}{e}\frac{\partial^2}{\partial z^2}C_{h,e}(z,t) + G_{A_{h,e}}(z,t) + G_{T_{h,e}}(z,t), \quad (20)$$

where n_d and n_a represent the concentration of donor and acceptor atoms, respectively; In Equation 18, $G_{A_{h,e}}(z,t)$ represents the avalanche generation rate of electrons and holes; and $G_{T_{h,e}}(z,t)$ represents the tunneling generation rate.

Due to the tunneling phenomenon, the electron and hole generation rate is expressed as Equations 21a–23,

$$G_{T_e}(z,t) = a_T E^2(z,t) e^{\left(1-\frac{b_T}{E(z,t)}\right)}, \quad (21a)$$

$$G_{T_h}(z,t) = G_{T_n}(z',t), \quad (21b)$$

$$\text{Here } a_T = \frac{e}{8\pi h^2}\left(\frac{m^*_{ef}}{E_g}\right)^{\frac{1}{2}}, \quad (22)$$

$$\text{And } b_T = \frac{1}{2eh}\left(\frac{m^*_{ef}}{2}\right)^{\frac{1}{2}}, \quad (23)$$

$$G_{A_{h,e}}(z,t) = \alpha_{h,e}(z,t)\vartheta_{h,e}(z,t)C_{h,e}(z,t), \quad (24)$$

$$\vartheta_{h,e}(z,t) = \frac{\mu_{h,e}E(z,t)}{1 + \frac{\mu_{h,e}E(z,t)}{\vartheta_{h,e}^{Sat}(z,t)}}. \quad (25)$$

In Equation 25, $\vartheta_{h,e}(z,t)$ represents the drift velocity of the charged carriers; $\mu_{h,e}$ represents the mobility of the charged carriers; and $\vartheta_{h,e}^{Sat}(z,t)$ represents the saturation velocity of the charged carriers.

In Equation 24, the ionization rate of electrons and holes is denoted by $\alpha_{h,e}(z,t)$, and it is calculated using the following expression.

$$\alpha_{p,n} = A_n e^{-\left(\frac{B_n}{E}\right)^m}. \quad (26)$$

In Equation 26, m represents the exponential co-efficient; A_n represents the pre-exponential electric field constant; and B_n represents the induced electric field constant.

The induced electric field $E(z,t)$ mentioned in Equations 21a, 21b and Equation 24 is obtained by Equation 27.

$$E(z,t) = \int_0^t \int_{z=0}^{z=W_{QRD}} \frac{e}{\epsilon}\rho(z,t)dzdt. \quad (27)$$

2.2 Design parameters

The width (W) and doping concentration (n_d) are two key factors for developing the MGL/SiNW exotic pin device in the THz frequency region. Therefore, the determination of the optimized width of the intrinsic region and the doping concentration of highly doped p and n regions are obtained by a number of computer runs. The amount of change in the doping concentration at the interfaces of the intrinsic region and the highly doped p and n regions can be obtained from Kundu et al. (2021a), Kundu et al. (2018), and Kundu and Mukherjee (2022).

$$\frac{\partial N}{\partial t} = D_{ef}\frac{\partial^2 N}{\partial x_n^2}. \quad (28)$$

At the steady-state condition, the solution to Equation 28 is given by

$$N(x_n') = N_0\left(1 - \frac{2}{\sqrt{\pi}}\int_0^{\lambda} e^{-\lambda^2}d\lambda\right), \quad (29)$$

where $\lambda = \frac{x_n'}{\sqrt{D_{ef}t}}$.

In Equation 29, x_n' represents the distance from the surface of the device; D_{ef} represents the effective diffusion constant; t represents the diffusion time; and N_0 represents the doping density of the impurity atoms.

The diffusion length ($L = \sqrt{D_{ef}t}$) is taken as 2–3 μm in this device modeling. The solution to Equation 29 is given in the Equation 30 and shown below.

$$N(x_n') = \pm N_h \exp\left(-1.08\lambda - 0.78\lambda^2\right). \quad (30)$$

In Equation 29, N_h denotes the doping concentration of the surface area. The value of the doping concentration of heavily doped p and n regions is obtained by

$$N(x_n) = N_a\left[exp\left(-\frac{x_n}{s}\right) - 1\right], \quad (31)$$

$$N(x) = N_d\left[1 - exp\left(\frac{x_n}{s}\right)\right], \quad (32)$$

where N_d represents the impurity concentration of the donor atoms; N_a represents the impurity concentration of the acceptor atoms; and s represents the exponential incremental factor for the doping concentration at the vicinity of the junction.

The value of s varies from 3.5 nm to 4.5 nm to calculate the doping concentration of p and n regions.

2.3 Non-linear RF characteristics

The study of the non-linear switching characteristics of the proposed device has been performed through the development of

the QRSP-DD model (coupled with a PSpice simulator). In this non-linear analysis, the large RF signal is applied to the developed QRSP-DD model by considering a 50% modulation index over the breakdown electric field. The switching performance, as well as the electrical characteristics of the DUT, is obtained by considering the iteration up to harmonics of the applied large RF signal, and it can be expressed as follows (Kundu et al., 2018):

$$x_l(t) = V \sum_{i=1}^{n-1} M_m^i \sin(2\pi f i t). \quad (33)$$

Equation 33 indicates the variation in the RF signal over the DC breakdown voltage. The equivalent circuit of nanowire SPST switches is analyzed at THz frequency by considering the voltage excitation approach of the non-sinusoidal RF signal. The component of large-RF-signal can be expressed as $M_m^i \sin(2\pi f i t)$. The precise investigation of non-linear switching behavior is taken by considering 2000 space steps and 400 time spaces with reproducibility and fidelity.

The V–I characteristics of the proposed DUT, which can be derived using Equation 34, yield the ideal values for DC current and breakdown voltage.

$$I_f = I_{sat}\tau\left[exp\left(\frac{qV}{KT} - 1\right)\right]. \quad (34)$$

Equation 34 denotes the reverse saturation current of the proposed DUT. The charged particles are injected into the intrinsic region under forward bias conditions. The product of the carrier lifetime (τ) and the current flowing across the DUT under forward bias conditions yields the number of injected charged particles (Q) (Kundu et al., 2018). These injected charged particles move toward the anode and cathode under the biasing conditions. However, some of the charged particles remain in the intrinsic region. It can be eliminated by applying a reverse recovery process. The reverse recovery mechanism causes the instantaneous reverse-transit current ($i(t)$) to begin flowing across the DUT. The transit-current component ($i(t)$) is an important factor in power dissipation in the DUT. Therefore, the analysis of the DUT's transit-time behavior is crucial for modeling the high-frequency device, and it can be represented as (Leenov, 1963)

$$i_t(t) = -I_m \exp\left[\frac{(t-T)}{\tau_{rrt}}\right] \text{at } t \geq T. \quad (35)$$

In Equation 35, τ_{rrt} represents the time constant of the reverse-recovery current component and I_m represents the maximum value of the same current component.

The solution to the 2-D carrier transport equation yields the RF resistance. The value of the RF resistance depends on the magnitude of the intrinsic region's resistance (R_{ir}) and the junction resistance ($R_{jr}(f)$) of the device. The expressions are provided as (Kundu and Mukherjee, 2022; Bellantoni et al., 1989) shown in Equations 36, 37.

$$R_{ir} = \left(\frac{KT}{q}\right)\left(\frac{W}{L}\right)\tan\left(\frac{W}{2L}\right), \quad (36)$$

$$R_{jr}(f) = \left(\frac{2KT}{qI}\right)\beta\tanh\left(\frac{W}{2L}\right)\cos\left(\varnothing - \frac{\theta}{2}\right). \quad (37)$$
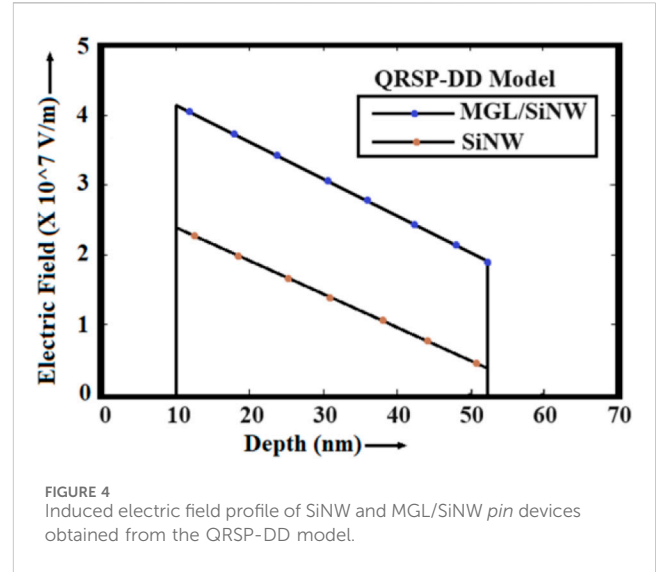
FIGURE 4
Induced electric field profile of SiNW and MGL/SiNW *pin* devices obtained from the QRSP-DD model.

Another important factor for the analysis of the switching behavior of the DUT is power dissipation (P_d), and it can be expressed as

$$P_{ds} = \frac{4R_s Z_0}{(Z_0 + 2R_s)^2} P_{av}. \quad (38)$$

In Equation 38, Z_0 is the characteristic-impedance of the device; P_{av} is the available RF power; I_d is the dissipated current; and C_j is the junction capacitance of the DUT.

Furthermore, the analysis of the SPST switch's switching characteristics in the RF frequency region of the electromagnetic spectrum considers all these significant device parameters. Employing the combination of the QRSP-DD model and PSpice simulator, the switching characteristics of the device are obtained, taking into account the appropriate values of parasitic elements (Figures 3A–C). The proposed device-based SPST switch with series-shunt and shunt configurations is shown in Figures 4A–C.

The expressions are provided as Kundu and Mukherjee, 2022; Bellantoni et al., 1989 shown in Equations 39–42.

$$IL(shunt) = 10\log_{10}\left(1 + \left(\frac{Z_0}{2X_c}\right)^2\right), \quad (39)$$

$$ISO(shunt) = 20\log_{10}\left(1 + \frac{Z_0}{2X_c}\right), \quad (40)$$

$$IL(series-shunt) = 10\log_{10}\left[1 + \left(\frac{R_s}{2Z_0}\right)^2 + \left(\frac{Z_0 + R_s}{2X_c}\right)^2\right], \quad (41)$$

$$ISO(series-shunt) = 10\log_{10}\left[1 + \left(\frac{Z_0}{2R_s}\right)^2 + \left(\frac{X_c}{2Z_0}\right)^2\left(1 + \frac{Z_0}{R_s}\right)^2\right]. \quad (42)$$

3 Results and discussion

In this section, the electrical characteristics of the DUTs and the performance of the switches are analyzed using the developed QRSP-DD model in conjunction with PSpice software. The
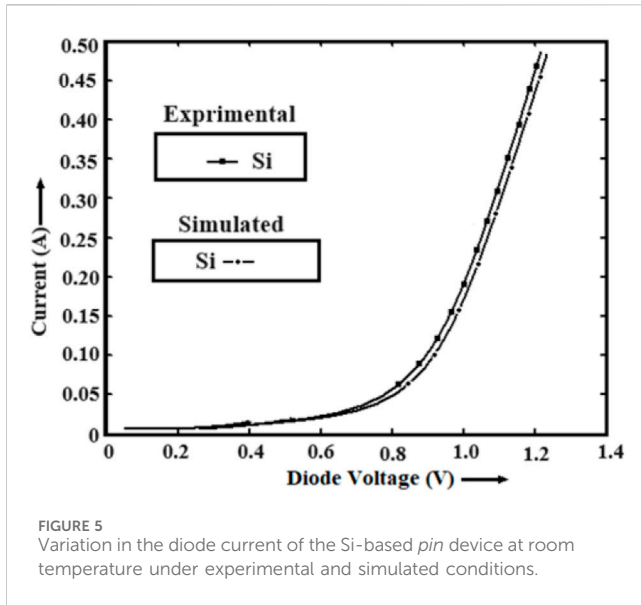
FIGURE 5
Variation in the diode current of the Si-based *pin* device at room temperature under experimental and simulated conditions.
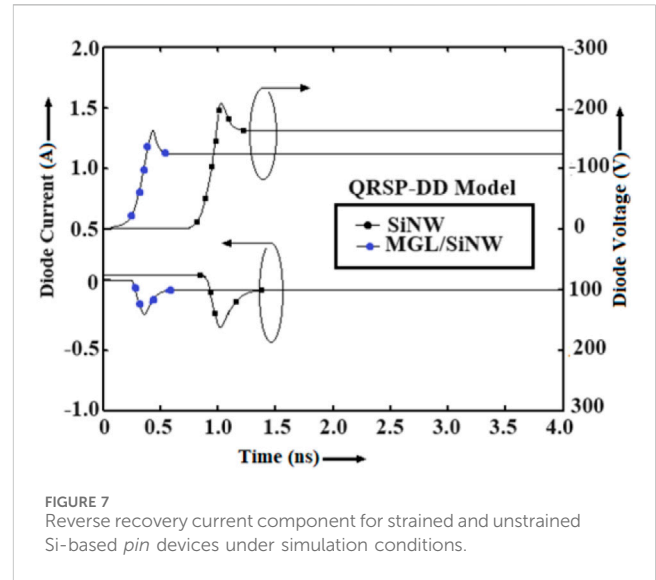
FIGURE 7
Reverse recovery current component for strained and unstrained Si-based *pin* devices under simulation conditions.
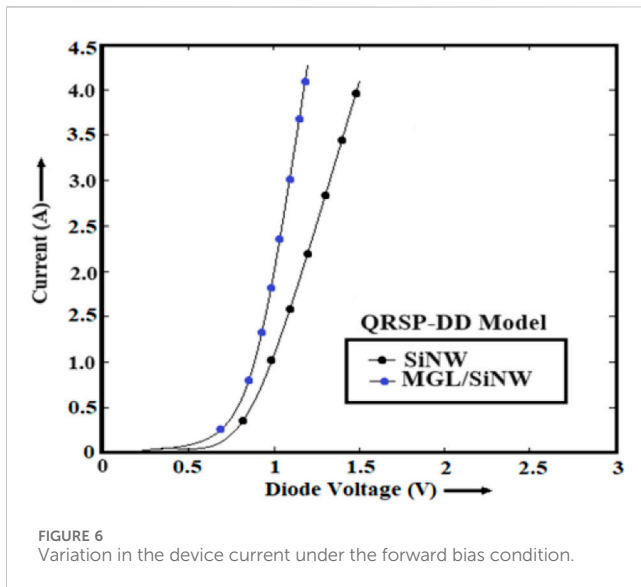
FIGURE 6
Variation in the device current under the forward bias condition.
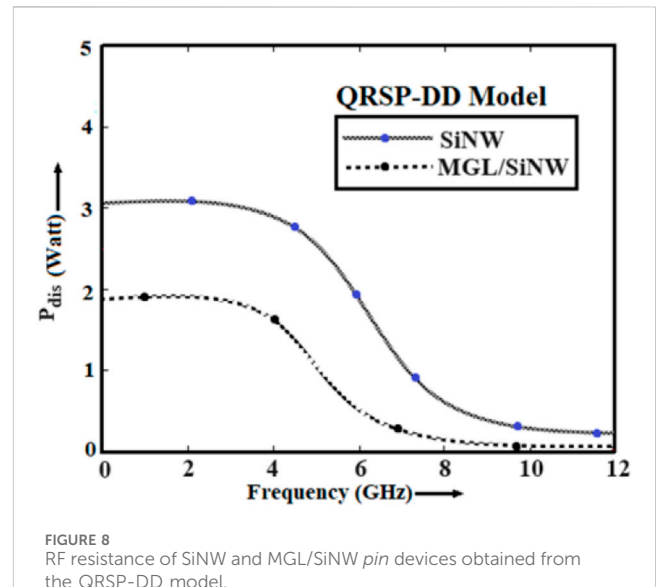
FIGURE 8
RF resistance of SiNW and MGL/SiNW *pin* devices obtained from the QRSP-DD model.

authors have also divided this section into two subsections to describe the results and analysis in detail.

3.1 Electrical characterization of the DUTs

In this section, the authors investigate the electrical characteristics of the DUTs. The induced electric field in the i-region plays an important role in the separation of the charged carriers and enhancement of the conductivity of the device. This phenomenon plays an important role in increasing the overall performance of the solid-state switch. It is analyzed for a complete period of oscillation, i.e., 0 to 2π, by considering the non-sinusoidal voltage-excitation method. The variation in the induced electric field is shown in Figure 4. It is observed from Figure 3 that in the case of a SiNW pin device, the magnitude of the electric field is $\times 2.2 10^7$ V/m, and in the case of MGL/SiNW pin devices, the magnitude of the electric field

is $\times 4.1 10^7$ V/m. The higher value of the electric field proves the superiority of the MGL/SiNW pin device compared to its SiNW counterpart. In this section, the authors have established the correctness/validity of the QRSP-DD model by analyzing the results obtained from the simulation and experimental conditions under similar circumstances. In this validation, the authors considered the flat structure-based pin device in the range of microwave frequency as no experimental result was found in the THz frequency domain. Under simulation and experimental conditions, the plots of V versus I characteristics of the Si-based pin device are shown in Figure 5 (Bogle et al., 2010). It is clear from Figure 5 that the obtained simulated data are almost identical to the reported experimental data. Hence, the correctness/validity of the QRSP-DD model is established. After establishing the correctness/validity of the QRSP-DD model, the electrical characteristics of the DUTs are studied in detail. At ambient temperature, the plot of V versus I of
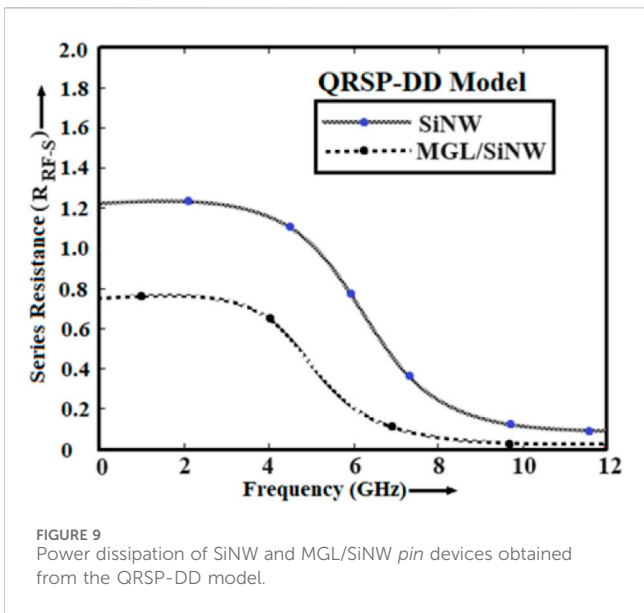
FIGURE 9
Power dissipation of SiNW and MGL/SiNW *pin* devices obtained from the QRSP-DD model.
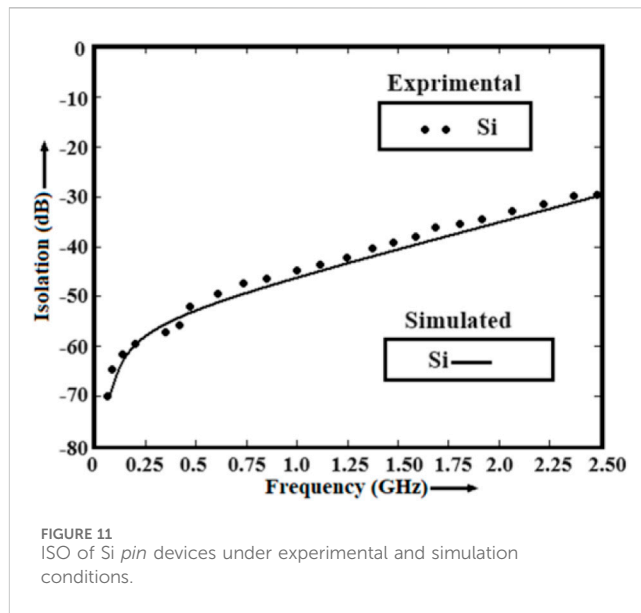
FIGURE 11
ISO of Si *pin* devices under experimental and simulation conditions.
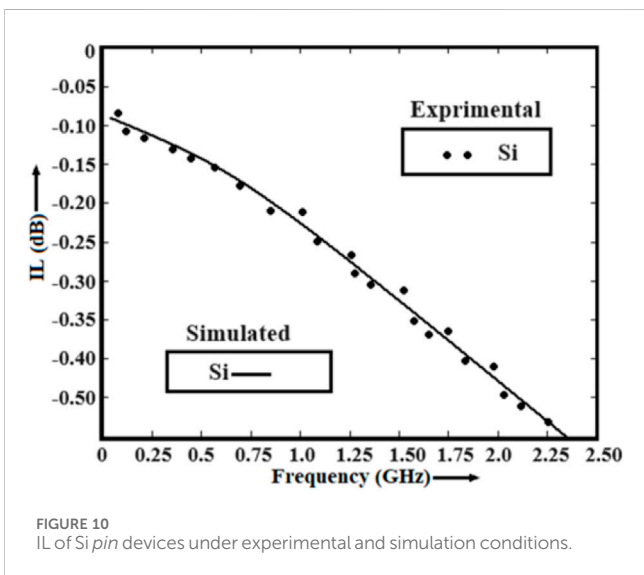
FIGURE 10
IL of Si *pin* devices under experimental and simulation conditions.
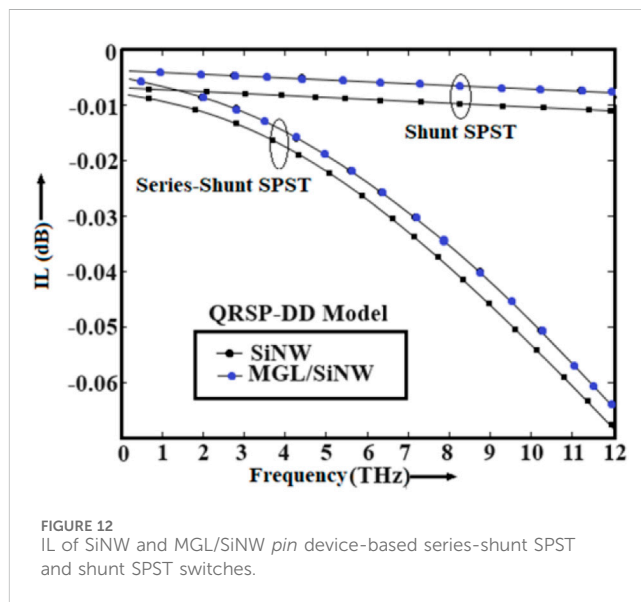
FIGURE 12
IL of SiNW and MGL/SiNW *pin* device-based series-shunt SPST and shunt SPST switches.

the SiNW and MGL/SiNW devices is shown in Figure 6. It is observed from Figure 6 that the MGL/SiNW pin device offers better results compared to its SiNW counterpart. The transit time analysis provides a clear understanding of the reverse recovery time. The transit time analysis of the proposed device is shown in Figure 7. It is observed from this transit time analysis that the reverse recovery time is 1.15 ns for the SiNW device and 0.4 ns for the MGL/SiNW device. From this observation, it is clear that the reverse recovery time is much shorter for MGL/SiNW devices compared to SiNW devices. The value of reverse recovery time indicates higher switching speed. This feature of the MGL/SiNW device is in favor of the THz frequency operation. The RF resistance plays an important role in the determination of insertion loss and isolation of the device. The performance of the device can be enhanced by reducing the RF resistance. In the intrinsic region of the DUTs, the variation in RF resistance to the corresponding frequency component is shown in Figure 9. It is

noticed from Figure 8 that the value of RF resistance is 1.17 Ω for the SiNW pin device and 0.56 Ω for MGL/SiNW at 4.6 THz. In the THz frequency domain, the variations in power dissipation of the designed devices are shown in Figure 9. As observed from Figure 9, the magnitude of power dissipation in the case of the MGL/SiNW is significantly smaller than that of its counterpart.

3.2 Analysis of the switching characteristics of the series-shunt SPST and shunt SPST, SPDT, and SPMT switches

In this section, the authors have investigated the switching characteristics of the series-shunt and shunt SPST switches. The switching characteristics of the devices are studied in the THz frequency domain in terms of IL and ISO using the PSpice
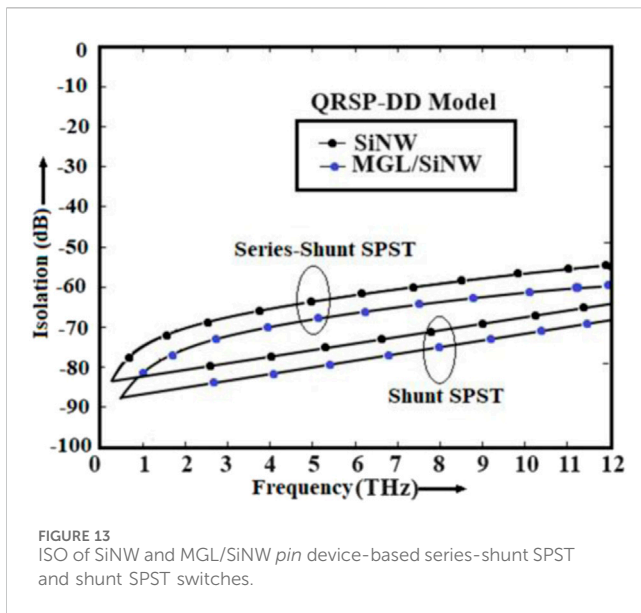
FIGURE 13
ISO of SiNW and MGL/SiNW *pin* device-based series-shunt SPST and shunt SPST switches.
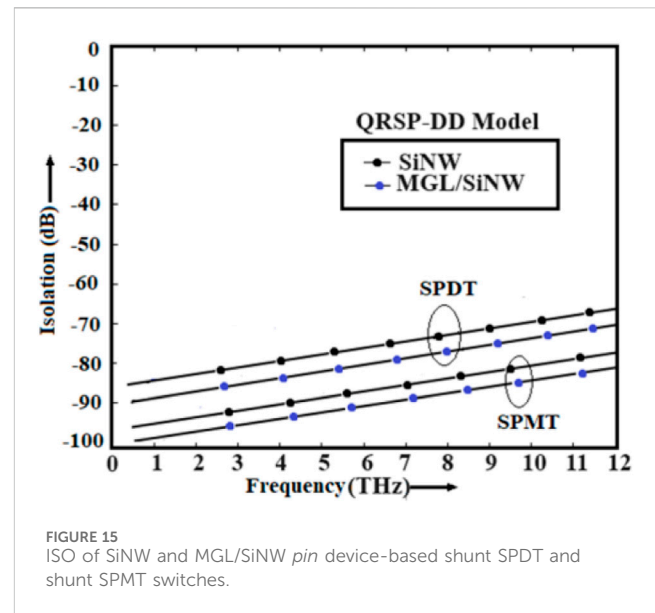
FIGURE 15
ISO of SiNW and MGL/SiNW *pin* device-based shunt SPDT and shunt SPMT switches.
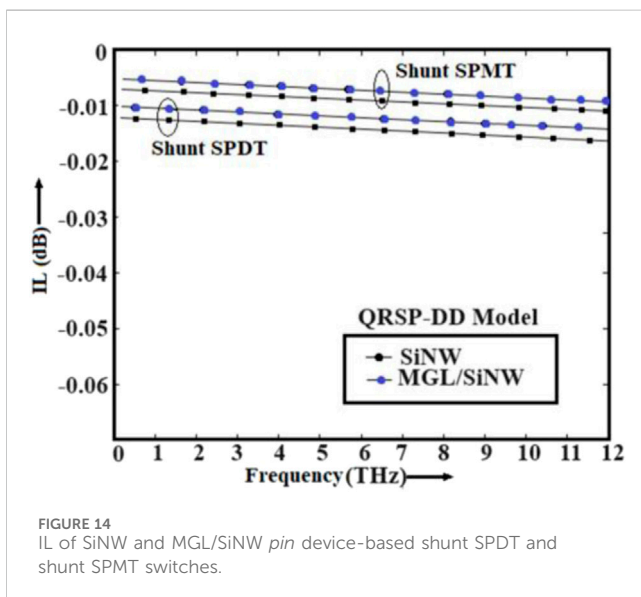
FIGURE 14
IL of SiNW and MGL/SiNW *pin* device-based shunt SPDT and shunt SPMT switches.

simulator coupled with the developed QRSP-DD model. The low insertion loss and high isolation can enhance the switching performance of the device at high-frequency operation. Hence, the optimization of these parameters is a challenging task for the device engineers. The authors have checked the model's validity by analyzing the experimental observations and simulated data obtained from the PSpice simulator coupled with the QRSP-DD model in a similar operating environment (Henfiner et al., 2001). The authors have used the same model to analyze the switching characteristics of the devices in the THz frequency domain. The experimental observations and simulated data of IL and ISO with the variations in frequency in the microwave region are shown in Figures 10, 11, respectively. It is observed from Figures 10, 11 that the simulated data taken from the QRSP-DD model are similar to the actual data obtained from experimental observation. The abovementioned study clarifies the superiority of the developed model. In addition, the switching

performance in terms of IL and ISO of the designed device-based series-shunt and shunt SPST switches are shown in Figures 12, 13, respectively, and shunt SPST and SPMT switches are shown in Figures 14, 15, respectively. It is observed from Figure 12 that the IL is 0.0052 dB at 5 THz frequency in the case of the MGL/SiNW-based shunt SPST switch. It is also observed from Figure 13 that ISO is −79.52 dB at 5 THz frequency in the case of the MGL/SiNW-based shunt SPST switch. The abovementioned discussion reveals the superiority of MGL/SiNW-based shunt SPST switches over their SiNW counterpart.

It is also observed from Figure 14 that the IL is significantly small (0.007 dB) at 5 THz frequency in the case of the MGL/SiNW-based shunt SPMT switch compared to the shunt SPDT switch. On the other hand, ISO is significantly high (91.15 dB) at 5 THz frequency in the case of the MGL/SiNW-based shunt SPMT switch, as observed in Figure 15. Hence, this investigation reveals the superiority of the MGL/SiNW-based SPMT switch in the THz frequency region.

4 Proposed fabrication model of the device

The authors established multi-graphene layer/Si nanowire pin-based series-shunt and shunt SPST, SPDT, and SPMT switches in the THz frequency range. The electrical characteristics of graphene make it suitable for switching applications in the THz frequency range.

The heterostructure graphene/Si nanowire switch can be fabricated using the molecular beam epitaxy (MBE) method, which allows the creation of abrupt and flat hetero-interfaces. From the maturity and cost efficiency perspective, Si (100) could be chosen as a substrate material for developing the epitaxial layer of graphene and Si according to the device's design. Ohmic contacts with low resistance could be developed using the plasma etching process, followed by the rapid thermal annealing (RTA) process.

Low-resistive metals like Ni/Ti/Au could be chosen for developing cathode terminals on the heavily doped n-type multi-graphene layer. Ni could be selected to develop the anode terminal on the heavily doped p-type multi-graphene layer. The mesa-structure of the device could be

FIGURE 16
Proposed fabrication model of the MGL/SiNW *pin* switch.

formed using photolithography and lift-off processes. The proposed fabrication model of the device is shown in Figure 16.

5 Conclusion

The performance of SiNW exotic MGL/SiNW pin device-based SPST, SPDT, and SPMT switches is analyzed in terms of insertion loss and isolation in the THz frequency domain. From this comprehensive study, it has been observed that exotic MGL/SiNW pin device-based SPMT switches offer low insertion loss and high isolation compared to their SiNW counterparts in the THz frequency domain. Hence, the superiority of the exotic MGL/SiNW pin switch is established for application in the THz frequency domain. This study is very useful in the field of device

engineering for the development of high-frequency switches and detectors.

Data availability statement

The original contributions presented in the study are included in the article/Supplementary Material; further inquiries can be directed to the corresponding author.

Author contributions

SB: writing–original draft and writing–review and editing. AK: writing–original draft and writing–review and editing. JK: writing–review and editing and writing–original draft. AS: writing–review and editing. MM: software, supervision, validation, and writing–review and editing.

Funding

Conflict of interest

The authors declare that the research was conducted in the absence of any commercial or financial relationships that could be construed as a potential conflict of interest.

Publisher's note

All claims expressed in this article are solely those of the authors and do not necessarily represent those of their affiliated organizations, or those of the publisher, the editors and the reviewers. Any product that may be evaluated in this article, or claim that may be made by its manufacturer, is not guaranteed or endorsed by the publisher.

References

Ang, K. W., Chui, K. J., Blimetsov, V., Du, A., Balasubramanian, N., Li, M. F., et al. (2004). Enhanced performance in 50 nm N-MOSFETs with silicon–carbon source/drain regions. IEDM technical digest. *IEEE Int. Electron. Dev. Meet.* doi:10.1109/IEDM.2004.1419383

Bellantoni, J. V., Bartle, D. C., Payne, D., McDermott, G., Bandla, S., Tayrani, R., et al. (1989). Monolithic GaAs p-i-n diode switch circuits for high-power millimeter-wave applications. *IEEE Trans. Microw. Theory Tech.* 37, 2162–2165. doi:10.1109/22.44137

Bogle, J. J., Hubert, R. J., and Boles, T. E. (2010). "A 50 watt monolithic surface-mount series-shunt pin diode switch with integrated thermal sink," in Proceeding of Asia-Pacific Conference, USA, 07-10 December 2010.

Boles, T., Brogl, J., and Hong, D., (2013). AlGaS anode hetero-junction pin diodes. *Wiley* 10, 786–789. doi:10.1002/pssc.201200612

Buder, T., Kinayman, T., and Yong-Hoon, Y. (2003). Low-loss high-isolation 60-80 GHz GaAs SPST pin switch. *IEEE MTT-s Dig.*, 1307–1310. doi:10.1109/MWSYM.2003.1212610

Camara., N., and Zekentes, H. (2006). Microwave pin diode and switches based on 4H-SiC. *IEEE Electron Device Lett.* 27, 108–110. doi:10.1109/LED.2005.862686

Egorov, I., Xiao, Y., and Poloskov, A. (2018). Pin diode diagnostics of pulsed electron beam for high repetition rate model. *J. Phys. Conf. Ser.* 830, 0120044. doi:10.1088/1742-6596/755/1/011001

Falco, C. D., Gatti, E., Lacaita, A. L., and Sacco, R. (2005). Quantum-corrected drift-diffusion models for transport in semiconductor device. *J. Comput. Phys.* 204, 533–561. doi:10.1016/j.jcp.2004.10.029

Greve, D. W. (2001). Si–Ge–C growth and devices. *Mater. Sci. Eng. B* 87 (3), 271–276. doi:10.1016/S0921-5107(01)00724-3

Hadi, M. H., Ahmad, B. H., and Shairi, N. A. (2013). "Effect of discrete pin diode on defected ground structure," in *Wireless technology and applications (ISWTA)", IEEE symposium*, 333–337.

Henfiner, A. R., Singh, R., Lai, J. S., Berning, D.W., Chapuy, C., et al. (2001). SiC power diode provide breakthrough performance for a wide range of application. *IEEE Trans.* 16, 273–278. doi:10.1109/63.911152

Johon, D. L., Pulfrey, D. L., and Castrol, L. C., (2004). Quantum capacitance in nanoscale device modelling. *J. Appl. Phys.* 96, 5180. doi:10.1063/1.1803614

Kundu, A., Bhattacharya, S., Chakraborty, D., Chakraborty, S., and Mukherjee, M. (2021b). Strain—engineered asymmetrical Si/Si1–xGex IR-photo-detector: theoretical

reliability and experimental feasibility studies. *IEEE Trans. Device Mater. Reliab.* 21 (4), 627–638. doi:10.1109/TDMR.2021.3125452

Kundu, A., Kanjilal, M., and Mukherjee, M. (2021a). Cubic versus hexagonal SiC vertical pin SPST/SPDT/SPMT switches for MMW communication systems: a modified quantum drift-diffusion model for switching characteristics analysis. *Microsyst. Technol.* 27, 387–406. doi:10.1007/s00542-019-04445-9

Kundu, A., Kanjilal, M. R., and Mukherjee, M. (2018). III-V super-lattice SPST/SPMT pin switches for THz communication: - theoretical and experimental feasibility studies. *Microsyst. Technol.* 27, 539–541. doi:10.1007/s00542-018-4053-5

Kundu, A., Kundu, J., Modak, D., and Mukherjee, M. (2019). Quantum modified drift-diffusion modeling of vertically doped asymmetrical pin switches for application in MMW system. *AIP Conf. Proc.* 2072. doi:10.1063/1.5090241

Kundu, A., and Mukherjee, M. (2022). Physics based non-linear large-signal analysis of multiple-graphene layer exotic *pin* (p^{++}–n^-–n–n^{++}) devices and ultra-fast SPST/SPDT/SPMT switches on Si/3C-SiC (100) substrates for application in THz-communication. *Microsyst. Technol.* 28, 683–704. doi:10.1007/s00542-019-04325-2

Leenov, D. (1963). —The silicon pin diode as a microwave rader protector at megawatt level. *IEEE Trans. Electron Devices* 10, 53–61. doi:10.1109/T-ED.1964.15283

Mamedes, D. F., and Bornemann, J. (2021). High-gain reconfigurable antenna system using PIN-Diode-Switched frequency selective surfaces for 3.5 GHz 5G application. *2021 SBMO/IEEE MTT-S Int. Microw. Optoelectron. Conf. (IMOC)*, 1–3. doi:10.1109/imoc53012.2021.9624918

Ng, M.-F., Zhou, L., Yang, S., Sim, L. Y., Tan, V. B. C., and Wu, P. (2007). Theoretical investigation of silicon nanowires: methodology, geometry, surface modification, and electrical conductivity using a multiscale approach. *Phys. Rev. B* 76, 155435. doi:10.1103/PhysRevB.76.155435

Novoselov, K. S., Geim, A. K., Morozov, S. V., Jiang, D., Zhang, Y., Dubonos, S. V., et al. (2004). Electric field effect in atomically thin carbon films. *Science* 306, 666–669. doi:10.1126/science.1102896

Oberlin, A., Endo, M., and Koyama, T. (1976). Filamentous growth of carbon through benzene decomposition. *J. Cryst. Growth* 32, 335–349. doi:10.1016/0022-0248(76)90115-9

Paz-Martínez, G., Trevino-Palacios, C. G., Molina-Reyes, J., Romero-Moran, A., Cervantes-Garcia, E., Mateos, J., et al. (2021). Influence of laser modulation frequency on the performance of terahertz photoconductive switches on semi-insulating GaAs exhibiting negative differential conductance. *IEEE Trans. Terahertz Sci. Technol.* 11 (5), 591–597. doi:10.1109/TTHZ.2021.3083926

Pinping, S., Wang, L., and Upadhyaya, U., (2005). High isolation 10HHz to 20GHZ SPDT switches design using novel octagonal pin diode structure. *Microelectron. Electron Devices WMED* 38, 15. doi:10.1109/WMED.2005.1431612

Pratt, I., and Oliver, M. (2021). "Performance of PIN diode RF switches within HF RFID reader designs," in 2021 IEEE International Conference on RFID Technology and Applications (RFID-TA), USA, 6-8 Oct. 2021, 289–292. doi:10.1109/rfid-ta53372.2021.9617334

Sze, S. M. (2008). *Semiconductor devices: physics and technology.* 2nd Edition. New York: Willey. doi:10.1002/0470068329

Takahashi, K., Okamura, S., Wang, X., et al. (2011). "A capacitance compensated high isolation and low insertion loss series pin diode SPDT switch," in *Proceeding of the 41st European microwave communication* (IEEE), 583–586. Available at: https://ieeexplore.ieee.org/document/6101964/.

Tomioka, K., Ikejiri, K., Tanaka, T., Motohisa, J., Hara, S., Hiruma, K., et al. (2011). Selective-area growth of III-V nanowires and their applications. *J. Mater. Res.* 26 (17), 2127–2141. doi:10.1557/jmr.2011.103

Tomioka, K., Kobayashi, Y., Motohisa, J., Hara, S., and Fukui, T. (2009). Selective-area growth of vertically aligned GaAs and GaAs/AlGaAs core-shell nanowires on Si(111) substrate. *Nanotechnology* 20 (14), 145302. doi:10.1088/0957-4484/20/14/145302

Xu, Y., Yuan, X., Ye, F., Wang, Z., Zhang, Y., Diab, M., et al. (2021). Impact of high switching speed and high switching frequency of wide-bandgap motor drives on electric machines. *IEEE Access* 9, 82866–82880. doi:10.1109/ACCESS.2021.3086680

Yang, Z., Yang, T., You, Y., and Xu, R. (2005). A 2GHz high isolation DPDT switches MMIC microwave proceeding. *APMC, Asia Parcific Conf. Proceeding* 2, 4–7. doi:10.1109/APMC.2005.1606503

Glossary

h	Planck's constant	N_d	impurity concentration of the donor atoms
$U_{unit\text{-}s}$	unit step function	l_m	position of the miniband
$m^*_{ef}(z)$	effective mass of the charged carrier	N_a	impurity concentration of acceptor atoms
$C_{p,n}(z,t)$	concentration of the charged carrier	ΔE_C^{offset}	offset present in the conduction band
n_d	concentration of donor atoms	S	exponential incremental factor for the doping concentration at the vicinity of the junction
$\psi(x,y,z)$	total wave function		
n_a	concentration of acceptor atoms		
$E_{ef}(z)$	effective energy term		
$G_{A_{h,e}}(z,t)$	avalanche generation rate of electrons and holes		
$\phi(z)$	effective potential		
$G_{T_{h,e}}(z,t)$	tunneling generation rate		
B_n^{QCDD}	Bohm potential		
$\vartheta_{h,e}(z,t)$	drift velocity of the charged carriers		
E_g	bandgap energy		
$\mu_{h,e}$	mobility of the charged carriers		
N_c	effective density state of the conduction band		
$\vartheta_{h,e}^{Sat}(z,t)$	saturation velocity of the charged carriers		
N_v	effective density state of the valence band		
$\alpha_{h,e}(z,t)$	ionization rate of electrons and holes		
$E_{def}(z)$	energy into the effective density state		
m	exponential co-efficient		
n	concentration of the negatively charged carrier		
A_n	pre-exponential electric field constant		
$m_{efz}^{*W_{wl}/B_r}$	effective mass of the charged carrier in the barrier region in the out-of-plane direction		
B_n	induced electric field constant		
$V_n^{W_{wl}/B_r}$	developed potential across the well and barrier region		
$E(z,t)$	induced electric field		
$m_{ef(x,y)}^{*W_{wl}/B_r}$	effective mass of the charged carrier in the barrier region the in-plane direction		
W	width of the i-region		
$E_{ef}^{W_{wl}/B_r}$	effective energy of the charged carrier in the well and barrier region		
n_d	doping concentration		
W_{wl}	well		
x_n'	distance from the surface of the device		
B_r	barrier		
D_{ef}	effective diffusion constant		
$q_n(x,y,z)$	periodicity of the Bloch function		
t	diffusion time		
$m_{efz}^*(z)$	position-reliant effective mass		
N_0	doping density of the impurity atoms		
$\varphi(E)$	wave vector		